Biofilm Feedbacks Alter Hydrological Characteristics of Fractured Rock Impacting Sulfidogenesis and Treatment

Yiwei Cheng,[†] Christopher G. Hubbard,[‡] Jil T. Geller,[†] Chunwei Chou,[†] Marco Voltolini,[†] Anna L Engelbrektson,[§,∥] John D Coates,[§,∥] Jonathan B. Ajo-Franklin,[†] and Yuxin Wu[*,†]

[†] Earth and Environmental Sciences Area, Lawrence Berkeley National Laboratory, Berkeley, California 94720-8099, United States [‡] Water Research Institute, Cardiff University, Cardiff CF10 3XQ, Wales, U.K. [§] Energy Biosciences Institute, and [∥] Department of Plant and Microbial Biology, University of California, Berkeley, California 94720, United States

*E-mail: ywu3@lbl.gov.

Abstract

Flow-through fractures dominate the movement of fluids in a variety of natural as well as engineered subsurface systems. Microbial activities in fractured rock impact subsurface energy recovery, storage, and waste disposal. It has been recognized that understanding how the contrasting permeability between fracture and matrix interacts with microbial metabolism under thermal and hydrological gradients is key to effective utilization of the subsurface, yet such studies are sparse. Microorganisms mediate the production of hydrogen sulfide (also known as souring) in oil-bearing geological formations. We conducted a comprehensive experimental study of a novel 2D fractured rock system to understand these complex interactions and demonstrated how biofilm development can impact fracture flow, which subsequently feedbacks to moderate sulfidogenesis. Elevated temperature relevant to reservoir conditions interacted with the injection of cold fluid and formed a thermal gradient away from fractures, creating thermal niches for microbial activities in the fractured rock. Results showed that while fracture flows were dominant in the beginning, with time, growth of the biofilm in the fractures reduced permeability, effectively moderating the initial fracture–matrix contrast, and limited microbial accessibility to nutrients and subsequent reactions rates.

1. Introduction

The Earth’s subsurface is intricately tied to world energy and water demands. In addition to serving as energy sources (i.e., hydrocarbon, geothermal), subsurface reservoirs also provide long-term storage options for waste generated from energy production (e.g., nuclear waste, carbon dioxide from burning of fossil fuels).(1−4) In subsurface formations, flow-through fractures often dominate the movement of fluids in the Earth’s crust.(5) Fractures and the surrounding rock matrix often differ markedly in hydraulic characteristics, that is, fracture permeability can be orders of magnitude higher than that of the matrix.(6) Simulations based on field data have revealed that flow partitioning between fractures and matrix is

dependent on the fracture–matrix permeability ratio as well as critical fracture aperture values above which flow transitions from matrix to fracture-dominated.(6) Differences in fracture–matrix flow regimes translate into chemical and thermal gradients between the fracture and the matrix. These thermal gradients occur when the injection fluid is of a different temperature than the host rock. Fluid flow velocity impacts the thermal gradient in near-fracture regions.(7) On a larger scale, the thermal gradients are further perpetuated by the distributions of fractures and network connectivity within the rock matrix, contributing to heterogeneity in abiotic and biotic reaction rates.

Microbes drive the cycling of major elements (e.g., hydrogen, carbon, oxygen, sulfur) on Earth(8) and mediate a wide range of reactions in the deep subsurface.(9) In addition to indigenous microbes, recent studies demonstrated the ability of non-indigenous microbes, typically introduced during fluid injection processes, to colonize hydraulically fractured rocks under harsh conditions.(10,11) Microbes form biofilms on surfaces of fractures and pore spaces within rock matrices. These biofilms are made of clusters of microbial cells tightly bound together by a matrix of extracellular polymeric substances (EPSs) secreted by the microbial cells. Biofilms can significantly modify the permeability of the system,(12−15) causing disruption in flow(16) and limiting mass transfer between the fracture and rock matrix.(17)

Microbial activities in fractured rock, both natural and engineered, that is, via injection of hydraulic fracturing fluids, have both positive and negative impacts on subsurface energy recovery, storage, and waste disposal.(10,11,18,19) During microbial enhanced hydrocarbon recovery (MEHR), promotion of biofilm growth strategically within the oil reservoirs can lead to improvement in yield. Also known as selective bioclogging, it is a process by which high-permeability and oil-depleted regions are clogged to divert flow toward low permeability and oil-rich regions, thus improving sweep efficiency.(19−21) On the other hand, recent investigation into microbial communities in the hydraulically fractured Marcellus and Utica shales revealed microbes mediating fermentation and thiosulfate reduction. Thiosulfate reduction leads to the production of sulfide and problems associated with reservoir souring.(10) Understanding how the contrasting permeability between the fracture and matrix interacts with microbial metabolism under heterogeneous thermal and hydrological gradients across a fracture–matrix interface is key to effective utilization of the subsurface (Figure 1).

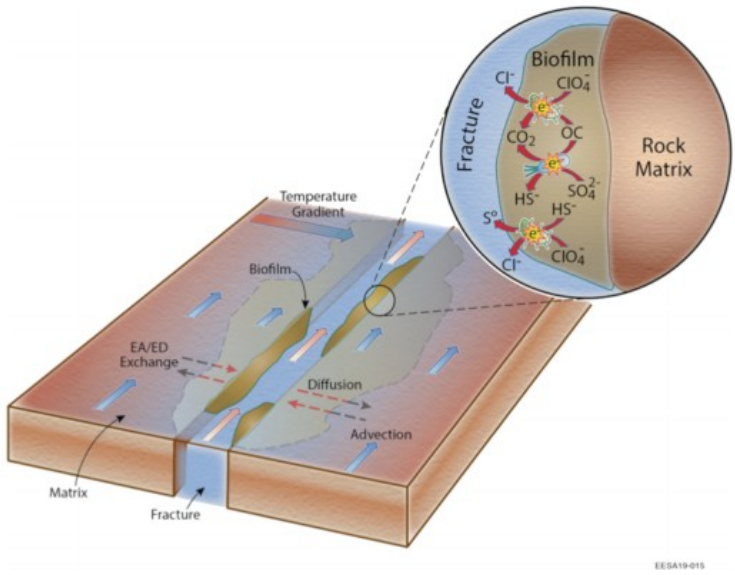

Figure 1. Schematic of interactions between the biofilm and the flow at the fracture/matrix interface as explored in this experiment. Abbreviations/chemicals shown in the figure: EA, electron acceptor; ED, electron donor; Cl^-, chloride; ClO_4^-, perchlorate; CO_2, carbon dioxide; OC, organic carbon; SO_4^{2-}, sulfate; HS^-, sulfide; S^0, elemental sulfur; e^-, electron.

Sulfate-reducing microorganisms (SRMs) mediate the reduction of sulfate to sulfide (souring) in oil-bearing rock formations when sulfate-rich seawater is injected during secondary production. To date, most of the experimental souring studies involving flow-through systems have used high-permeability homogeneous sand packs as the matrix material. Engelbrektson et al.(22) and Wu et al.(23) compared the effectiveness of different inhibitors (i.e., nitrate and (per)chlorate) on biogenic sulfide production and, in subsequent follow-up column studies, the impact of different inhibitor dosages.(24) The most recent is a 3D tank experiment by Cheng et al.,(25) which revealed the control that spatial distributions of hydrologic characteristics exert over reservoir souring and treatment. In contrast, subsurface systems are highly heterogeneous consolidated materials with lower matrix permeability and, in many cases, are also heavily fractured. In well-documented cases,(2) fracture corridors control the bulk of injected water and may generate a thermal field amenable to rapid souring.

Despite the potential importance of microbial activities in fractures, studies that explore the interactions and feedbacks between fracture–matrix flow, thermal gradient, biofilm formation, and reaction rates are nonexistent. Here, we present a comprehensive experimental study of a novel 2D fractured rock system to understand these complex interactions (Figures 1 and 2) and demonstrate how biofilm development can impact fracture flow, which subsequently feedbacks to moderate microbial reactions. By using tightly controlled fracture geometry, tailored thermal gradients, fluid chemistry, and microbial activities, we deconvolved the roles that fracture–matrix interactions, thermal gradients, and biofilms played in controlling subsurface microbially mediated biogeochemical processes. We used sulfur cycling, a process common in subsurfaces and important for hydrocarbon

recovery, as our model system (Figure 1). Specifically, SRMs were introduced to facilitate souring under simulated secondary oil production scenarios with the injection of sulfate-rich seawater into the fractured rock. Following successful sulfate reduction, chemical treatment with perchlorate and re-inoculation with perchlorate-reducing microbes (PRMs) were conducted to reverse the reactions. The thermal gradients in the system were perturbed to understand their impact on the microbial active zone and biogeochemical reaction rates across the fracture–matrix interface.

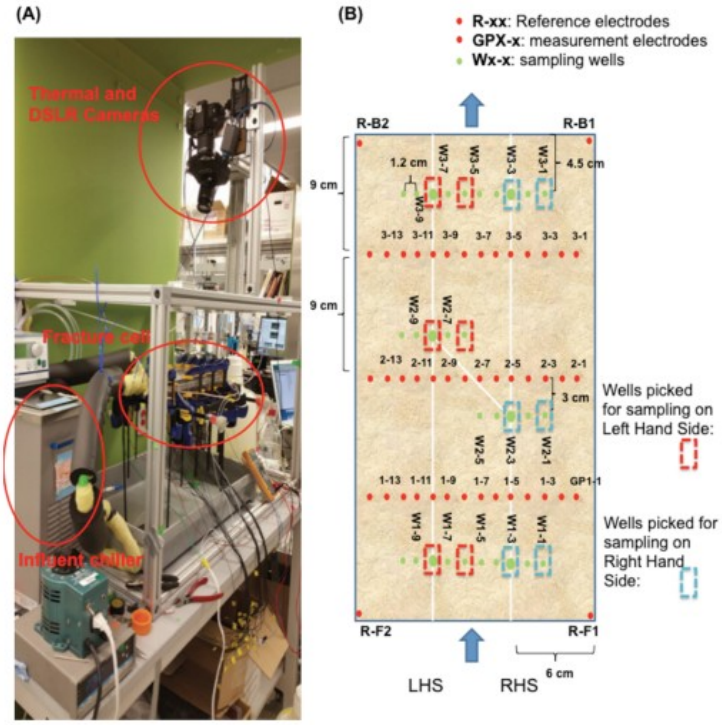

Figure 2. (A) Setup for the fractured flow cell biosouring and desouring experiment. The flow cell was constructed using a slab (36 cm long × 18 cm wide × 1 cm thick) of quarried Kirby sandstone. Temperatures of the heating elements were set at 70 °C to mimic conditions in deep oil reservoirs. Before reaching the fracture cell, the influent fluid was chilled to 5 °C using a water bath to simulate injection of seawater, mimicking secondary oil recovery in offshore environments such as the North Sea. Thermal and DSLR cameras were mounted 0.55 m above the experimental setup to capture time-lapse thermography and time-lapse optical images of the flow cell respectively. (B) Schematic aerial view of the fractured flow cell showing fluid sampling locations.

2. Methods

2.1. Experimental Setup and Operation

A quasi-two-dimensional flow cell was constructed using a slab (36 cm long × 18 cm wide × 1 cm thick) of quarried Kirby sandstone (porosity ≈ 0.15, gas permeability ≈ 10 mDarcy, mD) as a simplified model of the fractured sandstone reservoirs in the North Sea oilfields.(2,26) Three straight fractures were cut into the sandstone: two long and parallel fractures along the length and flow direction of the sandstone (both 36 cm long, aperture: ~1 mm and ~0.8 mm), and one short fracture (~9 cm long, aperture: ~1 mm) at a 45° angle connecting the two long parallel fractures (Figure 2). Fracture apertures were controlled using a small number of borosilicate glass beads of known sizes deposited toward the bottom of the fracture before

application of a lateral load; these “spacer” beads did not obstruct fracture flow due to their small number and limited vertical extent. The fractured sandstone slab was encased in clear, chemical- and temperature-resistant polycarbonate plates. A 3 mm-thick PDMS layer was installed between the sandstone and polycarbonate plate on each side to provide a surface seal. Small stainless steel-based heating elements were installed on both sides (parallel to the long fractures) of the fractured rock for temperature manipulation. Temperatures of the heating elements were set at 70 °C to mimic conditions in deep oil reservoirs. Pressure transducers were installed at the influent and effluent ends of the fractured flow cell to monitor changes in differential pressure of the system. Pressure data were logged every 30 s and used to quantify permeability change over time.

Solution made from Instant Ocean (Spectrum Brands) (40 g L^{-1}, ∼28 mM sulfate) was used as the saturating media as well as the carrier fluid for nutrients and treatments. The selection of Instant Ocean was made to simulate secondary recovery with seawater flooding and to evaluate the effects of high salinity and complex water chemistry on the souring process and the effectiveness of the treatments. Acetate (10 mM) was also added to the saturating media as the carbon source. In addition, 6 mM NH_4Cl, 0.4 mM KH_2PO_4, trace minerals, and Thauer’s vitamins were added to the saturating media to ensure no macro- (N and P) or micronutrient limitations on microbial growth during the experiment. This solution mix was injected into the fractured cell throughout the experiment. Subsequently, 10 mM perchlorate was injected into the fractured cell during the treatment period. This treatment period started once effluent sulfide concentration was relatively stable. Application of perchlorate as souring treatment was examined in previous studies.(22,24) Specifically, perchlorate has been shown to be an effective alternative to nitrate. Perchlorate can directly inhibit microbial sulfate reduction. The presence of perchlorate triggers competition between heterotrophic perchlorate reducers (hPRMs) and SRMs for limited electron donors, effectively reducing sulfate reduction. Perchlorate reducers (PRMs) also mediate the reduction–oxidation (REDOX) pathway that couples the reduction of perchlorate to the oxidation of sulfide.

All solutions were filter-sterilized using 0.2 μm filters and kept under a nitrogen headspace (1–2 psi) throughout the experiments to maintain an anaerobic environment similar to deep subsurface flow systems including oil reservoirs. The flow rates were regulated with peristaltic pumps and maintained at ∼0.8 mL min^{-1} throughout the experiments. Before reaching the fracture cell, the influent fluid was chilled to 5 °C using a water bath to simulate injection of seawater; this temperature was chosen to simulate secondary oil recovery in North Sea offshore environments. Perchlorate treatment in the fractured rock started once significant amounts of sulfide were consistently measured in the sampling wells and the effluents with colorimetric methods.(27,28)

The flow cell was first flooded with deionized water followed by a sequence of tracer tests. Two tracer tests conducted before the flow cell inoculation elucidated the hydrological characteristics. First, a pulsed fluorescent dye tracer study was conducted. In the first pulsed fluorescent dye tracer test, the tracer (100 mg fluorescein sodium/L) was injected for 40 min at ~1 mL/min. In the second test, a bromide tracer was continuously administered for a duration of 2 h at ~1.0 mL/min.

The flow cell was inoculated with an SRM-containing microbial community on day 0 (phase A, day 0 being the start of the souring phase). The microbial community was enriched from San Francisco bay mud with acetate as the electron donor following earlier studies.(24,25) After inoculation, the flow was paused for 11 days to allow the microbial community to establish. Flow was resumed on day 11. On day 90, 10 mM perchlorate was added to the influent solution. On day 152, a temperature manipulation experiment was conducted by shutting off the right-side heater for 3 weeks (21 days). During this period, left heating elements was set at 70 °C while the right heating element was turned off. A similar flow rate and water chemistry were maintained through the temperature manipulation period. A PRM community was introduced into the system on day 181. After inoculation, the flow was paused till day 222 to allow the PRM community to establish within the flow cell. The experiment concluded on day 281. Details on the timing and the different phases of the experiment are outlined in Table1.

Table 1. Different Phases of the Experiment

day	phase	description
		initial saturation of the flow cell with medium
0	A	SRM inoculation followed by shut in
11	B	start flow—sulfidogenesis phase
90	C	addition of 10 mM perchlorate
152−173	D	thermal manipulation
181	E	PRM inoculation followed by shut in
222	F	flow restarted
281		experiment completed

2.2. Image Acquisition and Image Analysis

Figure 2A shows the experimental setup. A thermal camera (FLIR, Ax5) was mounted 0.55 m above the experimental setup to capture time-lapse thermography of the flow cell. Direct temperature readings were measured with six type-T thermocouples (accurate to 0.1 °C) installed at equal intervals apart between the two heating elements. We established a calibration between FLIR data and measured the temperature by directly relating FLIR data at a pixel to the corresponding thermocouple measurement (Figure S1); the calibration accommodates the unknown emissivity of the top system surface. In addition to the thermal camera, a DSLR camera (Canon, EOS Rebel T3i, 8 megapixel) was also installed above

the flow cell to record time-lapse optical images of the flow cell every half an hour (Figure 2A).

We performed image analysis on the DSLR recorded images of the near-fracture region. Imageries showed the development/growth of gray/black zones throughout the flow cell (see Results). Post-experimental analysis revealed that the black material was related to biological (biofilm) activity (see XRPD and EDS Results below). To evaluate the temporal changes in the overall intensity of the surface biological activities, we took advantage of the contrast between the light brown sandstone and the darkened reaction zone and quantified the grayness in the fracture proximity. Optical images were read in and converted to grayscale: each pixel was assigned a grayness value between 0 (white) and 1 (black). The spatial region of interest was defined and cropped out as the interface within a 2-pixel distance from the fractures (~37.15 cm^2). For each 3 h stacked image, we calculated the mean grayness value of all the pixels in the near-fracture region (Figure S2). All images were processed in R,(29) an open source programming language commonly used in scientific analysis.

2.3. Sampling and Analysis

Effluent liquids were collected from the end of the fractured cell throughout the experiment. To capture spatiotemporal changes in chemical characteristics, liquids were also sampled from a network consisting of 30 sampling micro-ports distributed throughout the flow cell (Figure 2B). During sampling events, approximately 0.5 mL of fluid was extracted, filtered (0.2 μm), and measured for sulfide, anion, and dissolved iron (acidified to 0.1 M HCl). Influent samples were also collected at the start of each influent replenishment. Dissolved sulfide concentrations were immediately analyzed using colorimetric techniques.(27,28) Anion samples (sulfate, perchlorate, and acetate) were analyzed by ion chromatography (Dionex DX120). For microbial analysis, effluent samples were spun down at 14,000 × *g* for 10 min, and DNA was isolated from the pellet using a DNeasy Powersoil kit (Qiagen, Valencia, CA). The samples were then analyzed for microbial community composition following the method used by Carlstrom et al.(30) Briefly, primer sets MiSeq 16S F and Miseq 16S R were used to amplify a 287 bp region of the 16S rRNA gene. PCR conditions were as follows: 95 °C for 3 min; 30 cycles of 95 °C for 30 s, 64 °C for 30 s, and 72 °C for 30 s; and 10 min at 72 °C.(30) Library preparation was done using the Nextera XT Index kit (Illumina, Hayward, CA) following manufacturer's protocol, and samples were quantified and pooled in equal concentrations. MiSeq sequencing was performed by the DNA Technologies Core at the UC Davis Genome Center (Davis, CA). Samples were demultiplexed and analyzed using Mothur.(31) Sequences were aligned, quality-filtered, clustered into 97% OTUs, and classified using the RDP and SILVA databases.

2.4. Sandstone Mineral and Chemical Characterization

Sections of the fractured sandstone were extracted for mineralogical and chemical characterization. X-ray powder diffraction (XRPD) was performed on samples using a Rigaku SmartLab system equipped with a Cu X-ray source. Measuring conditions were 40 kV and 44 mA of current, and data were scanned in the 4–70° 2θ range. Quantitative Rietveld analysis was carried out with the MAUD software.(32) Selected samples were also examined using a Zeiss EVO-LS10 SEM (scanning electron microscope), with a tungsten filament source and capable of operating at variable pressure in the sample chamber; imaging was conducted using both secondary electron (SE) and back-scattered electron (BSE) detectors. The instrument is also equipped with an energy-dispersive X-ray spectroscopy (EDS) detector (Oxford Instruments X-MAX 20 mm^2), allowing us to perform semi-quantitative chemical analyses on the most interesting areas of the sample.

3. Results

3.1. Flow and Geochemical Trends

Two tracer tests conducted before the flow cell inoculation elucidated the hydrological characteristics of the system before microbial activities. First, a pulsed fluorescent dye tracer study was conducted. In the first pulsed fluorescent dye tracer test, the tracer (100 mg fluorescein sodium/L) was injected for 40 min at ~1 mL/min. Results showed that a breakthrough began 4 min after injection and peaked at 20 min followed by a quick drop off in concentration at 27 min. A second peak was observed at 36 min before the concentration slowly decreased below the detection limit (Figure S3). In the second test, a bromide tracer was continuously administered for a duration of 2 h at ~1.0 mL/min. The tracer broke through at 27 min after injection. Thereafter, effluent bromide concentrations increased to a steady state value of 80% of the injection concentration (Figure S3).

Injection of simulated seawater containing high sulfate concentrations, 28.9 ± 1.7 mM (mean ± 1σ, n = 43), amended with acetate, 10.1 ± 0.6 mM (n = 31), as the organic donor, resulted in sulfate reduction in the fractured rock system (Figure 3). During the souring phase, effluent sulfate concentrations decreased to mean values of 27.9 ± 1.6 mM (mean ± 1σ, n = 45) up to day 181 (inoculation of PRMs followed by shut in). At the same time, effluent sulfide concentrations increased to mean values of 1.9 ± 0.9 mM (mean ± 1σ, n = 45) up to day 181 (inoculation of PRMs followed by shut in). During souring, effluent acetate slowly decreased to 8.7 ± 0.6 mM (mean ± 1σ, n = 43) up to day 181 and, thereafter, rapidly decreased to 0 mM until the end of the experiment. When perchlorate was initially introduced into the system (influent = 9.8 ± 2.1 mM, n = 27), no observable changes in sulfide, sulfate, and acetate concentrations were detected. Effluent perchlorate concentration remained similar to influent concentration, at 9.9 ± 2.1 mM (mean ± 1σ, n = 26) up to day 181. After shut in and PRM inoculation, it was observed that effluent sulfate concentrations rebounded (25.7 ± 1.2 mM, n = 4) close to influent concentrations (26.2 ± 0.3 mM, n = 6) with a concurrent

decrease in sulfide, acetate, and perchlorate concentrations (reduced to 4.4 ± 2.2 mM, n = 5). In addition to effluent samples, liquid samples were also collected from 12 sampling wells within the fractured flow cell (Figure 2). Throughout the experiment, consumption of effluent sulfate and corresponding production of effluent sulfide follow a 1:1 ratio (Figure S4A). A similar 1:1 relationship was also observed for consumption of effluent acetate and corresponding production of effluent sulfide (Figure S4B). Temporal trends of the geochemical species (i.e., sulfate, sulfide, and perchlorate) as revealed by the samples from the sampling wells bore resemblance to the respective effluent trends (Figure S5).

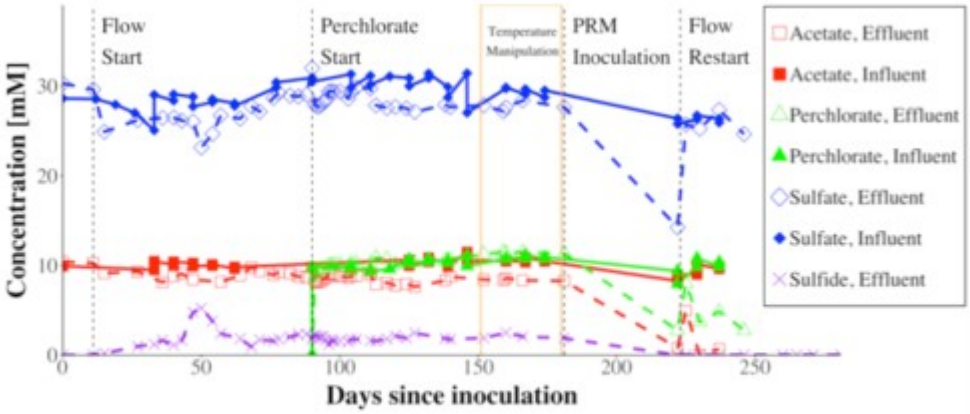

Figure 3. Dissolved sulfide, sulfate, acetate, and perchlorate concentrations in influent and effluent samples.

3.2. Microbiology

Changes in treatment affected the microbiology in the system (Figure 4). Initially, the system was dominated by organisms capable of sulfate reduction and those capable of other metabolisms such as fermentation. The sulfate-reducing community varied from 11 to 71% of the total microbial community depending upon the day and was made up primarily of *Desulfomicrobium*, *Desulfotignum*, and *Desulfobacter*. Even after perchlorate was applied (on day 90), there was very little change in community structure. The perchlorate-reducing community consisting of potential perchlorate reducers was essentially nonexistent until day 222 (first microbial sampling day after inoculation of perchlorate-reducing community) when a perchlorate-reducing community was added to the cell (Figure 4A,C). After that point, perchlorate reducers from the genera *Sedimenticola* and *Marinobacter* dominated the community, with the total potential perchlorate reducing community ranging from 24.2% before shut in (day 181) to 85.0 ± 9.0% of the total community after shut in.

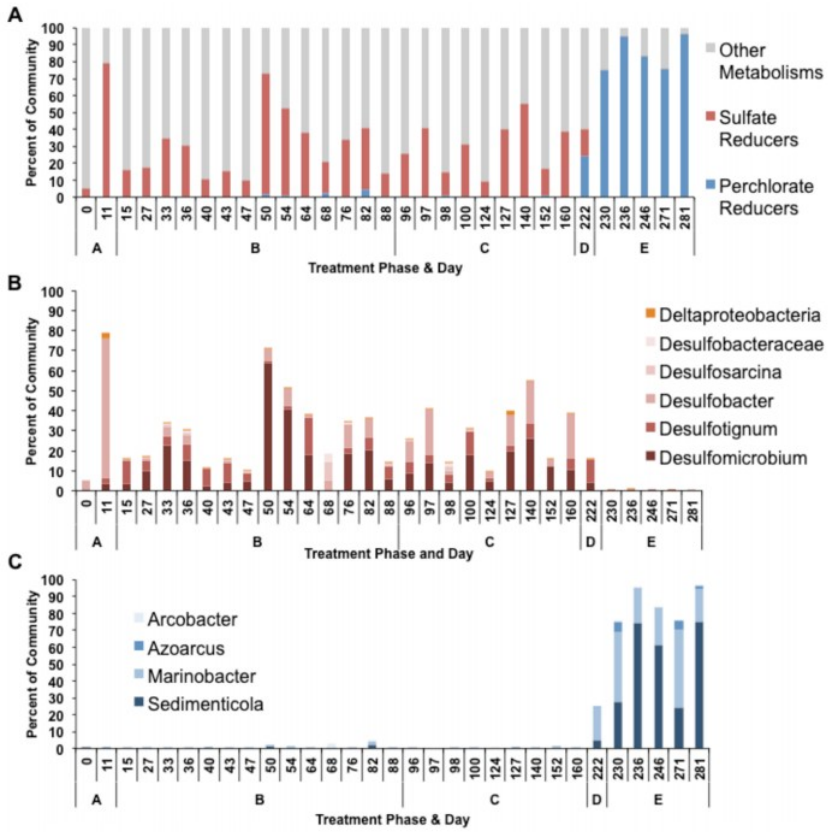

Figure 4. Microbial community results. (A) Percentage of community catalyzing sulfate reduction, perchlorate reduction, and other metabolisms. (B) Families of sulfate-reducing microorganisms across the experiment. (C) Families of perchlorate-reducing microorganisms across the experiment.

3.3. Thermal and DSLR Images

Thermal imagery revealed the temperature pattern before the water injection began. The highest temperature values (70 °C) were at the edges of the flow cell where the heaters were located. Temperature decreased towards the center of the flow cell, reaching a value of 30 °C (Figure 5A). The injection of cold water (5 °C) into the heated sandstone slab reduced the temperature of the system. The highest temperatures (48 °C) were observed at the edges of the flow cell, while the lowest temperatures (20 °C) occurred at the center (Figure 5B). During the temperature manipulation phase at day 152, the highest temperature values (48 °C) were located at the left edge, and the temperature decreased going toward the right edge of the cell, reaching a low value of (20 °C) (Figure 5C).

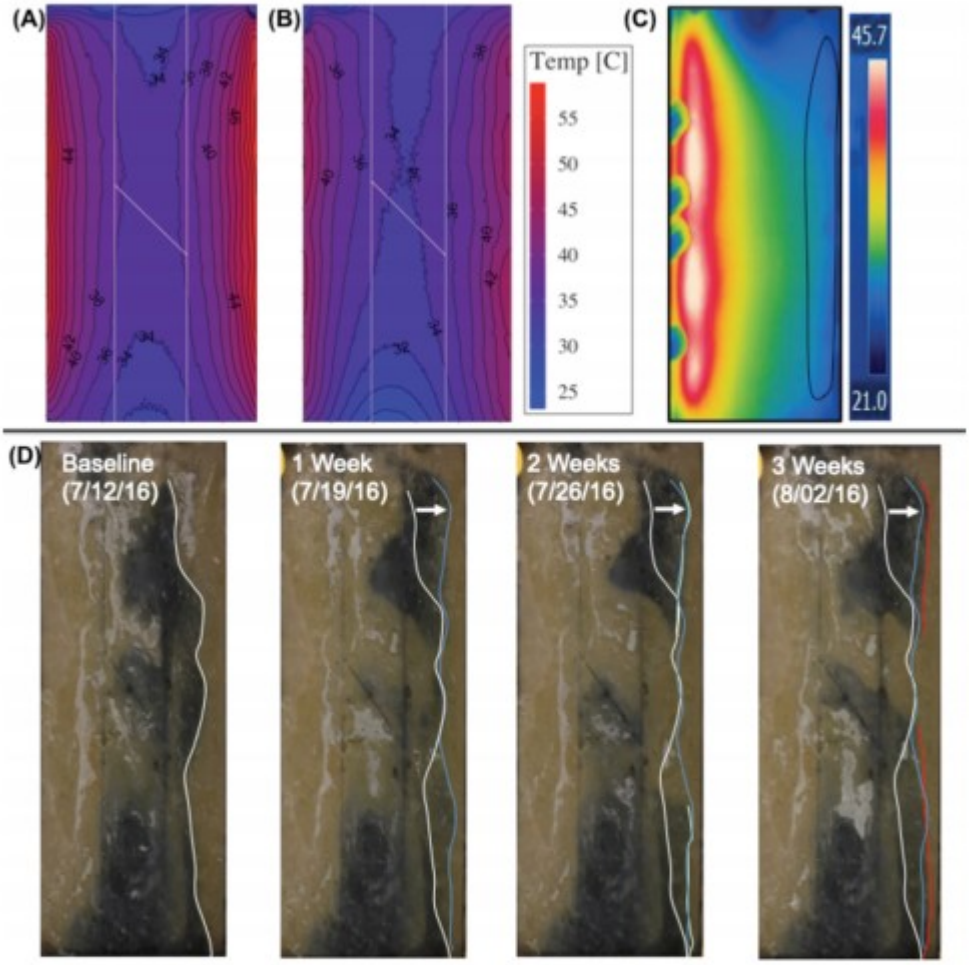

Figure 5. Thermal maps of the fractured flow cell: (A) before flow, (B) during flow, and (C) during the thermal manipulation phase when the right heater was switched off. (D) DSLR images of the fractured cell during the thermal manipulation phase. The reactive biological zone (black regions in images) shifted into the mesophilic region on the side of the flow cell during thermal manipulation phase.

Real-time imagery showed the development/growth of black “mass” starting from the fractures, slowly propagating throughout the flow cell. It was observed that the biological mass mainly occupied the region in between the two main parallel fractures and near the inlet. Post-experimental analysis revealed that the black material was related to biological (biofilm) activity (see XRPD and EDS Results below). This reactive biological zone shifted into the mesophilic region on the side of the flow cell during the thermal manipulation phase when one heater was turned off (Figure 5D).

3.4. XRPD and EDS Results

XRPD Rietveld analysis on the Kirby sandstone revealed the following mineralogy (percentage by weight): quartz (89.3%), K feldspar (3.4%),

plagioclase (3.3%), illite and smectite (2.2%), and kaolinite (1.8%). SEM and EDS analysis carried out on the samples after dismantling the cell revealed the biofilm grown in the larger fracture, which appeared as a black material. Similar analysis was performed on a horizontal section cut from the sandstone slab with staining of the black mass (Figure 6f). In Figure 6f, the red circle highlights the location where the biofilm sample was collected, while the section of the slab scanned with the SEM is marked with the red rectangle. The fragments of biofilm under the SEM appeared as a gelatinous layer, covered with halite crystals, due to the evaporation of fluid after cell destruction, as displayed in Figure 6d. A portion of the sample without those crystals, when imaged with SEM secondary electrons, in Figure 6c, better highlighted the structure of this biofilm, at higher magnification. An EDS analysis of this part of the sample (Figure 6b) highlighted the organic nature of the sample, with carbon (C) and oxygen (O) being the most abundant element. The presence of chloride (Cl), and in part of sodium (Na), was related to the evaporation of the brine. The amount of sulfur (S) was relatively high, and a minor amount of iron (Fe) was detected. The color of this biofilm was thought to be related to a small fraction of flocculated amorphous Fe sulfide, and the EDS analysis seems to confirm this hypothesis. On the section of the sandstone (imaged using a mixed signal of secondary and backscattering electrons) as shown in Figure 6e, we carried out EDS mapping (Figure 6a) to try to evaluate the distribution of the biofilm in the pore space. Silicon (Si) and aluminum (Al) were observed in the distribution of the mineral components of the sandstone, with quartz and feldspar grains and coatings consisting of clays (highlighted by the Al map). The C map captured the distribution of the biofilm, with the Fe and S maps possibly related to the Fe sulfide flocculate distribution related to the bacterial activity. The C map suggested that the biological material was scattered in the whole sample as small zones and it did not agglomerate in specific pores or patches. These distributions seem to suggest that the biological activity is somewhat uniformly distributed (at this scale) in the pores of the material.

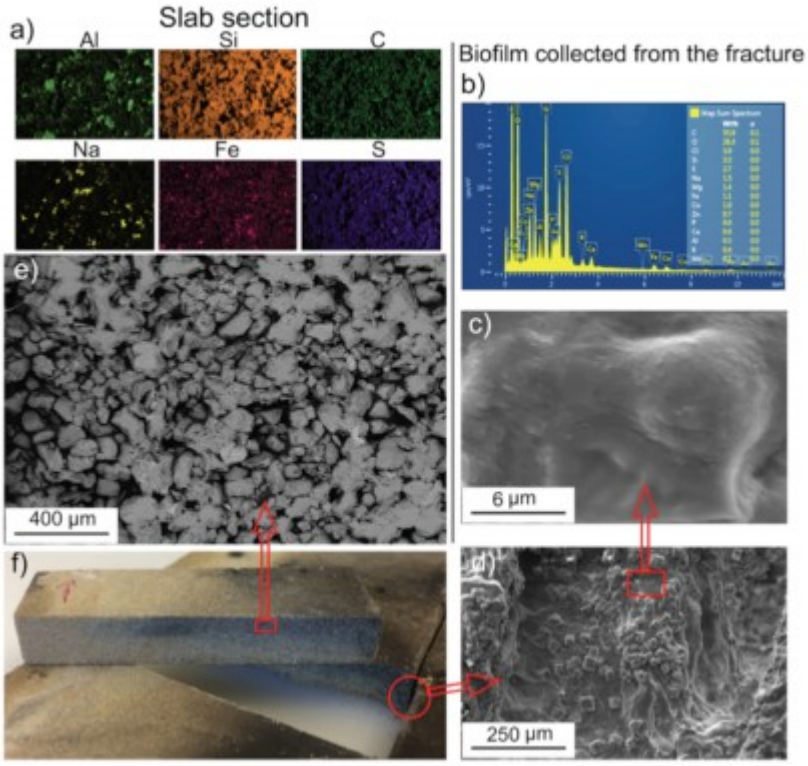

Figure 6. (a, e) On a section of the sandstone, we carried out EDS mapping to try to evaluate the distribution of the biofilm in the pore space. Silicon (Si) and aluminum (Al) are observed in the distribution of the mineral components of the sandstone, with quartz and feldspar grains and coatings consisting of clays (highlighted by the Al map). The C map captures the distribution of the biofilm, with the Fe and S maps possibly related to the Fe sulfide flocculate distribution related to the bacterial activity. (b) EDS analysis highlights the organic nature of the sample, with carbon (C) and oxygen (O) being the most abundant elements. The presence of chloride (Cl) and sodium (Na) is related to the evaporation of brine. Sulfur (S) is relatively high, and a minor amount of iron (Fe) is present. (c) A portion of the sample without those crystals, when imaged with SEM secondary electrons, shows the structure of this biofilm at higher magnification. (d) The fragments of biofilm under the SEM appear as a gelatinous layer, covered with halite crystals, due to the evaporation of fluid after cell destruction. (f) SEM (scanning electron microscopy) and EDS (energy-dispersive X-ray spectroscopy) analyses were performed on a horizontal section cut from the sandstone slab with staining of the black mass. The red circle highlights the location where the biofilm sample was collected, while the section of the slab scanned with the SEM is marked with the red rectangle (see a and e).

3.5. System Permeability and DSLR Images

Pressure transducers were installed at the influent and effluent ends of the fractured flow cell to monitor changes in differential pressure of the system as a possible result of occlusion of flow paths by biological material

accumulation. System permeability as calculated from pressure data (averaged over 3 h) showed an oscillatory trend with amplitude dampening throughout the experimental period (Figure 7A). For example, system permeability initially began at ~180 mD and decreased to ~10 mD at day 45. At day 50, permeability values rebounded to 165 mD and subsequently decreased to 75 mD at day 85.

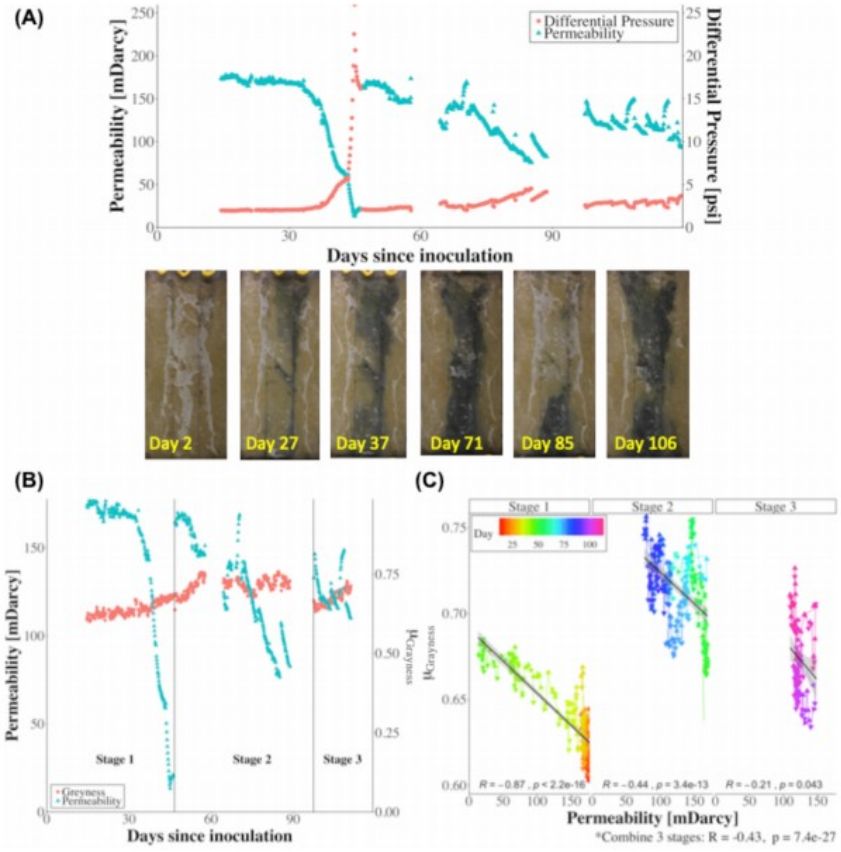

Figure 7. (A) System permeability as calculated from pressure data showed an oscillatory trend with amplitude dampening throughout the experimental period. Real-time (DSLR) images showed cyclic expansion and contraction of the biological zones within the flow cell. (B) Time series of permeability and mean grayness value of all the pixels in the near-fracture region ($\mu_{grayness}$). (C) Correlation between the degree of grayness of the fracture cell and permeability at different periods of the experiment showed the correlation to be always negative: the lower the permeability, the darker the fractured cell. However, the values of slopes were different for different time periods, indicating reduced sensitivity in permeability to darkening of the fracture cell.

Real-time (DSLR) images clearly showed cyclic expansion and contraction of the biological zones within the flow cell (Figure 7A). Generally, the cyclic expansion and contraction of the biological zone is out of phase with the permeability trend (Figure 7B). Image analysis of the degree of grayness revealed three distinct biomass expansion stages during which the mean grayness value increased. We further divided the permeability data into the same three stages (based on the distinctive drops in permeability): stage 1 (day 1–45), stage 2 (46–85), and stage 3 (beyond day 100). Statistical analysis showed negative correlation between darkening of the fracture cell and the increase in permeability (Pearson correlation $r(570) = -0.43$, $p < 0.001$, Figure 7B). However, the correlation was much stronger initially

($r(226) = -0.87$, $p < 0.001$) than later stages (stage 2 (day 46 to 85), $r(246) = -0.44$, $p < 0.001$; and stage 3 (beyond day 100), $r(94) = -0.21$, $p = 0.043$). Further analysis of correlation between the degree of grayness of the fracture cell and permeability at different periods of the experiment showed the correlation to be always negative: the lower the permeability, the darker the fractured cell. However, the values of slopes were different for different time periods, indicating reduced sensitivity in permeability to darkening of the fractured cell (Figure 7C). It was also observed that during the three distinct expansion phases, a counter-clockwise movement was observed in the correlation plot (Figure 7C), suggesting that expansion in the biomass preceded the drop in permeability.

4. Discussion

4.1. Microbial Mechanisms on Sulfate and Perchlorate Reduction

In an earlier study, construction of 16S rRNA gene libraries of microorganisms in produced water from the North Sea oil reservoir showed the presence of the genera *Acrobacter*, *Anaerophaga*, *Desulfovibrio*, *Desulfomicrobium*, *Thermotoga*, *Thermosipho*, *Haloanaerobium*, and *Spirochaeta*, which were also detected in oil-related samples in earlier studies.(33)*Desulfovibrio* and *Desulfomicrobium* are well known sulfate reducers, while members of *Haloanaerobium* have been known to mediate anaerobic fermentation. In other studies, microbial community analysis revealed the presence of heterotrophic and chemolithotrophic sulfate-reducing and nitrate-reducing bacteria in nitrate-treated North Sea oilfield microbial community composition.(26)

In this study, trends in the geochemical data coupled with the microbial community analysis yielded insights into the dynamics of sulfur cycling and the different mechanisms by which perchlorate inhibits sulfate reduction across the different treatment phases (Table1). Souring enriched for sulfate-reducing communities. Even with the injection of perchlorate, microbial community analysis indicated no known perchlorate-reducing groups being enriched in the community and no associated loss of perchlorate and that the SRMs continued to be the dominant groups during this period (Figure 4A), suggesting that the SRM community in the current study seems to be resistant to perchlorate toxicity at the 10 mM concentration. In a recent chemostat experiment involving sulfidogenic microbial communities exposed to various concentrations of perchlorate (i.e., 20, 50, and 80 mM), SRMs exposed to 80 mM perchlorate showed the most significant reduction in sulfide production, while the SRM exposed to 20 mM perchlorate showed little reduction in sulfide production by comparison.(34) Aside from impacting flow characteristics of the system, cells in biofilms behave differently from their counterparts in the planktonic phase. Case in point, the high viscosity of the biofilm matrix limits delivery of chemicals to the cells, indirectly conferring resistance to inhibitors. Studies have shown that biocides and

perchlorate are less effective against microbial biofilms than planktonic cells.(34,35)

After shut in and PRM inoculation, it was observed that effluent sulfate concentrations rebounded (close to influent concentrations) with a concurrent decrease in sulfide, acetate, and perchlorate concentrations. These trends suggest the actions of the perchlorate-reducing sulfide oxidation pathway(36) and bio-competition between heterotrophic perchlorate-reducing microorganisms (hPRMs) and SRMs for acetate. Indeed, the microbial analyses indicated the presence of *Sedimenticola* and *Marinobacter* OTUs (Figure 4A,C) within the community with the total potential perchlorate reducing-community that make up 85.0 ± 9.0% of the total community after shut in. Both *Sedimenticola*(37,38) and *Marinobacter*(39−41) are known hPRMs. Significant reduction in acetate suggests bio-competition to be the major mode of inhibition. Results from this study mirror observations from earlier experimental studies.(24,25)

4.2. Effects of Flow on Development of Thermal Gradients and Biological Reaction Zone

In this experiment, a shift in thermal field occurred in response to injection of cold water and impacted the spatial distribution of microbial communities. Initial (background) reservoir temperature and injection fluid (as controlled by the fractured network) interacted to control thermal gradient formation from fractures through rock matrices. Mesophilic (10–43 °C) zones surrounded the fracture and inlet regions, while the thermophilic (38–78 °C) zones were regions further away from the fracture network. Real-time imagery showed the development of biological mass starting from the fractures, slowly propagating throughout the flow cell. It was observed that the biological mass mainly occupied the region in between the two main parallel fractures and near the inlet, corresponding to the mesophilic temperature (10–43 °C) niche. The biological mass expanded in response to the change in thermal regime during the thermal manipulation phase: into the mesophilic region on the side of the flow cell with the heater turned off (Figure 5D). In oil reservoirs, thermal gradients can create spatial thermal niches for SRM communities of different sulfate-reducing capacities and sensitivities to inhibitors.(42) Recent studies in oil reservoir settings have highlighted the role that temperature plays in affecting the efficacy of the nitrate injection as treatment to curb sulfate reduction.(43−45)

It was noted that during the thermal manipulation phase, no changes to the effluent sulfide concentration was observed. Analysis showed that the left fracture (wider aperture) showed higher sulfide (paired t test, H_A: $\mu_d > 0$, $p = 0.0036$) and lower sulfate (paired t test, H_A: $\mu_d < 0$, $p = 0.0137$) and acetate (paired t test, H_A: $\mu_d < 0$, $p = 0.025$) concentrations than the right fracture (Figure 8). The narrower right-side fracture aperture, together with the reduction in fracture permeability due to biofilm (see below), offered a possible explanation as to why despite the expansion of biological mass

during heater manipulation, no significant amount of sulfide increased in the effluent. With larger fracture apertures or a denser fracture network coupled with higher rates of fluid flow, we can expect changes to effluent sulfide during thermal manipulation.

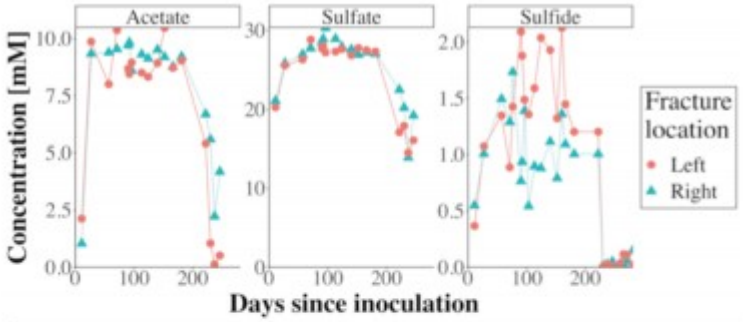

	Paired t-test results (paired by days since inoculation)					Left fracture statistics		Right fracture statistics	
	H_a (one-tail)	df	t	p value	Significance	Mean [mM]	Stdev [mM]	Mean [mM]	Stdev [mM]
Acetate	Left < Right	16	-2.12	0.025	*	6.91	3.60	7.72	2.79
Sulfate	Left < Right	16	-2.43	0.014	*	24.34	4.94	25.33	4.41
Sulfide	Left > Right	23	2.95	0.004	**	1.05	0.76	0.76	0.54

Figure 8. Analysis showed that the left fracture (wider aperture) showed higher sulfide (paired t test, H_A: $\mu_d > 0$, $p = 0.0036$) and lower sulfate (paired t test, H_A: $\mu_d < 0$, $p = 0.0137$) and acetate (paired t test, H_A: $\mu_d < 0$, $p = 0.025$) concentrations than the right fracture.

4.3. Biofilm Impact on System Permeability

Information from the light spectrum as recorded using a digital camera was processed and utilized as a proxy (degree of grayness) for the development of the biofilm. Despite sampling from a small zone within the larger sample, EDS analysis of the “blackish” biofilm sample highlighted the organic nature of the sample and the presence of a fair amount of Fe and S. The black coloration of the biofilm could be attributed to the presence of FeS precipitates, as confirmed by PXRD analysis. It was also noted that when the samples were left in an open atmosphere, with time, the black coloration was lost, possibly indicating the re-oxidation of the FeS, as was observed in prior experimental studies.(46) Biofilms have been found to bioaccumulate barium (Ba) and facilitate the formation of barite in marine environments in which Ba concentrations are prohibitively low.(47) A similar mechanism may be at work in this study where biofilms bioaccumulate Fe, facilitating the formation of FeS. The degree of grayness seems to be a good proxy for biofilm development, capturing the initial exponential development trend of the biofilm during the first 50 days, which corresponded to the exponential rise of effluent sulfide during the same time period (Figure S2). The use of light as a means of non-destructive biofilm assessment was performed by Ross et al.(48) during an experiment involving a glass–fracture plane. Specifically, reductions in light transmittance (occlusion of light by biofilm) were measured as a proxy for biofilm development. Specifically, results were expressed as the difference between the light transmittance recorded at time t and the initial light transmittance recorded at $t = 0$.

In this study, real-time DSLR images coupled with differential pressure data revealed the influence of biofilms on system permeability. Oscillations in permeability could potentially be due to the growth and detachment in the biofilm. A similar process has been suggested to describe results as observed in a biofilm modeling study conducted by Bozorg et al.(49) whose model was based on data from an earlier bioclogging experiment conducted in a partially inoculated sandbox conducted by Kildsgaard and Engesgaard.(50) The ubiquitous influence of biofilms on key processes of subsurface natural and engineered systems has been observed in previous studies.(16,51) However, this is the first time such cyclic expansion and contraction of the biological mass has been recorded visually at this scale. Further, it could be explained that during the detachment process, the loss of biofilm led to the inability to bioaccumulate Fe, resulting in the dissolution of FeS, which is visually observed as “discoloration” during the experiment.

Biofilm clogging of porous media had been previously demonstrated.(19,52,53) In this study, the cyclic expansion and contraction of the biological mass was shown to be generally out of phase with the permeability (Figure 7B). However, the negative correlation between permeability and darkening was strongest in the beginning (of souring). Similar to earlier experimental studies, reduction in permeability is linked to increasing microbial reaction rates.(53,54) In the study of Arnon et al.,(53,54) the microbial reaction was the biodegradation of 2,4,6-tribromophenol. Meanwhile, in our study, it was sulfate reduction, as clearly shown by the increase in effluent sulfide concentration to ~6 mM up to day 50. This suggests the main role that fractures play in sulfate reduction (in comparison to matrix), particularly in the early stages of the experiment. In support of the idea that fractures are the main loci of microbial activities, real-time imagery showed that the development of biological mass began from the fractures. Moreover, dissolved chemical species (i.e., sulfate, acetate) lost to the matrix by diffusion were available to bacteria (average size of ~1 μm) since the size of the majority of pore throats in sandstone is typically 1–10 μm (in comparison to 0.03–2 μm in tight-gas sandstones).(55) This explains the slow expansion of biomass into the matrix region surrounding the fractures.

This experiment differed from earlier studies and provided additional insight into system characteristics after fractures became clogged by biofilms. Beyond day 50, system permeability never returned to initial values (Figure 7). This suggests that biofilms modulate the fracture/matrix permeability ratio such that the initial fracture-dominant flow transitioned toward a more homogeneous flow across the fracture–matrix domains throughout the rest of the experiment. This was further demonstrated by the weaker relationship between permeability and biomass expansion in the later stages. The system transitioning impacted the biogeochemical dynamics of the system, resulting in steady-state production of sulfide (~2 mM) in the later phase of the experiment (before HPM inoculation).

5. Conclusions

Our experimental work offers a comprehensive view of the thermal, hydrological, and microbial interactions in the fracture–matrix, using microbial sulfate reduction as a model system. Results also showed that while fractures do exert strong control on flow and reaction rates, biological feedbacks in the near-fractured region can be equally important. Specifically, fractures may initially act as fast flow paths and loci of microbial reactions, but with clogging, reaction zones may become decentralized to small and localized zones within the fractured flow cell; however, these are most likely within the fractures or immediate vicinities. As such, the system transitions from that mediating higher microbial reaction rates to that of a lower capability. Case in point, initial fast delivery of nutrients through the fractures showed the system to produce high concentration of sulfide. However, after clogging, microbial sulfate reactions likely became localized to small pockets within the flow cell. The high sulfide plume coming out of these “hot spots” becomes diluted when mixed with fluid from other regions that bypassed high sulfate reduction zones. Results continue to support the idea that biofilm feedback can dampen initial fracture–matrix contrast and weaken fracture flow contributions to overall system behavior. This study also shows that microscale processes at the fracture–matrix interface can control macroscale behavior and because of biofilm moderation, heterogeneous reactions within the system can average out to a steady state behavior.

Acknowledgments

This work was funded by the Energy Biosciences Institute. The authors would like to thank the reviewers for their constructive comments.

References

(1) Witherspoon, P. A.; Cook, N. G.; Gale, J. E. Geologic storage of radioactive waste: Field studies in Sweden. Science 1981, 211, 894. (2) Barr, D.; Savory, K. E.; Fowler, S. R.; Arman, K.; McGarrity, J. P. Pre-development fracture modelling in the Clair field, west of Shetland. Geological Society, London, Special Publications. 2013, 270, 205. (3) Depaolo, D. J.; Orr, F. M., Jr. Geoscience research for our energy future. Phys. Today. 2008, 61, 46. (4) Vengosh, A.; Jackson, R. B.; Warner, N.; Darrah, T. H.; Kondash, A. A critical review of the risks to water resources from unconventional shale gas development and hydraulic fracturing in the United States. Environ. Sci. Technol. 2014, 48, 8334. (5) Pyrak-Nolte, L. J.; Nolte, D. D. Approaching a universal scaling relationship between fracture stiffness and fluid flow. Nat. Commun. 2016, 7, 10663. (6) Matthai, S. K.; Belayneh, M. Fluid flow partitioning between¨ fractures and a permeable rock matrix. Geophys. Res. Lett. 2004, 31, 19027. (7) Doe, T., Mclaren, R., Dershowitz, W. Discrete Fracture Network Simulations of Enhanced Geothermal Systems. Proceedings, 39th Workshop on Geothermal Reservoir Engineering,2014, 1−11, https:// pangea.stanford.edu/ERE/pdf/IGAstandard/SGW/2014/Doe.pdf.

(8) Falkowski, P. G.; Fenchel, T.; Delong, E. F. The microbial engines that drive earth’s biogeochemical cycles. Science 2008, 320, 1034−1039. (9) Lovley, D. R.; Chapelle, F. H. Deep subsurface microbial processes. Rev. Geophys. 1995, 33, 365. (10) Daly, R. A.; Borton, M. A.; Wilkins, M. J.; et al. Microbial metabolisms in a 2.5-km-deep ecosystem created by hydraulic fracturing in shales. Nat. Microbiol. 2016, 1, 16146. (11) Borton, M. A.; Hoyt, D. W.; Roux, S.; et al. Coupled laboratory and field investigations resolve microbial interactions that underpin persistence in hydraulically fractured shales. Proc. Natl. Acad. Sci. U. S. A. 2018, 115, E6585−E6594. (12) Cunningham, A. B.; Characklls, W. G.; Abedeen, F.; Crawford, D. Influence of Biofilm Accumulation on Porous Media Hydrodynamics. Environ. Sci. Technol. 1991, 25, 1305−1311. (13) Taylor, S. W.; Jaffe, P. R. Biofilm growth and the related changes´ in the physical properties of a porous medium: 1. Experimental investigation. Water Resour. Res. 1990, 26, 2153−2159. (14) Taylor, S. W.; Milly, P. C. D.; Jaffe, P. R. Biofilm growth and the´ related changes in the physical properties of a porous medium: 2. Permeability. Water Resour. Res. 1990, 26, 2161−2169. (15) Taylor, S. W.; Jaffe, P. R. Biofilm growth and the related changes´ in the physical properties of a porous medium: 3. Dispersivity and model verification. Water Resour. Res. 1990, 26, 2171−2180. (16) Drescher, K.; Shen, Y.; Bassler, B. L.; Stone, H. A. Biofilm streamers cause catastrophic disruption of flow with consequences for environmental and medical systems. Proc. Natl. Acad. Sci. U. S. A. 2013, 110, 4345−4350. (17) Charbonneau, A.; Novakowski, K.; Ross, N. The effect of a biofilm on solute diffusion in fractured porous media. J. Contam. Hydrol. 2006, 85, 212−228. (18) Surasani, V. K.; Li, L.; Ajo-Franklin, J. B.; Hubbard, C.; Hubbard, S. S.; Wu, Y. Bioclogging and permeability alteration byL. mesenteroidesin a sandstone reservoir: A reactive transport modeling study. Energy Fuels 2013, 27, 6538−6551. (19) Thullner, M.; Mauclaire, L.; Schroth, M. H.; Kinzelbach, W.; Zeyer, J. Interaction between water flow and spatial distribution of microbial growth in a two-dimensional flow field in saturated porous media. J. Contam. Hydrol. 2002, 58, 169−189. (20) Gullapalli, I. L.; Bae, J. H.; Hejl, K.; Edwards, A. Laboratory Design and Field Implementation of Microbial Profile Modification Process. SPE Reservoir Eval. Eng. 2000, 3, 42−49. (21) Kim, D.-S.; Fogler, H. S. Biomass evolution in porous media and its effects on permeability under starvation conditions. Biotechnol. Bioeng. 2000, 69, 47−56. (22) Engelbrektson, A.; Hubbard, C. G.; Tom, L. M.; et al. Inhibition of microbial sulfate reduction in a flow-through column system by (per)chlorate treatment. Front. Microbiol. 2014, 5, 315. (23) Wu, Y.; Cheng, Y.; Hubbard, C. G.; Hubbard, S.; Ajo-Franklin, J. B. Biogenic sulfide control by nitrate and (per)chlorate − A monitoring and modeling investigation. Chem. Geol. 2018, 476. (24) Engelbrektson, A. L.; Cheng, Y.; Hubbard, C. G.; et al. Attenuating sulfidogenesis in a soured continuous flow column system with perchlorate treatment. Front. Microbiol. 2018, 9, 1575. (25) Cheng, Y.; Wu, Y.; Wen, H.; et al. Microbial Sulfate Reduction and Perchlorate Inhibition in a Novel Mesoscale Tank Experiment. Energy Fuels 2018, 32, 12049−12065. (26) Bødtker, G.; Lysnes, K.; Torsvik, T.; Bjørnestad, E. Ø.; Sunde, E. Microbial

analysis of backflowed injection water from a nitrate-treated North Sea oil reservoir. J. Ind. Microbiol. Biotechnol. 2009, 36, 439−450. (27) Cline, J. D. Spectrophotometric Determination of Hydrogen Sulfide in Natural WATERS1. Limnol. Oceanogr. 1969, 14, 454−458. (28) Cord-Ruwisch, R. A quick method for the determination of dissolved and precipitated sulfides in cultures of sulfate-reducing bacteria. J. Microbiol. Methods 1985, 4, 33−36. (29) R Core Team R: A language and environment for statistical computing; R Foundation for Statistical Computing: Vienna, Austria URL http://wwwR-project.org/. 2013. (30) Carlström, C. I.; Lucas, L. N.; Rohde, R. A.; Haratian, A.; Engelbrektson, A. L.; Coates, J. D. Characterization of an anaerobic marine microbial community exposed to combined fluxes of perchlorate and salinity. Appl. Microbiol. Biotechnol. 2016, 100, 9719−9732. (31) Schloss, P. D.; Westcott, S. L.; Ryabin, T.; et al. Introducing mothur: Open-source, platform-independent, community-supported software for describing and comparing microbial communities. Appl. Environ. Microbiol. 2009, 75, 7537−7541. (32) Lutterotti, L.; Matthies, S.; Wenk, H. R. MAUD: a friendly JAVA program for material analysis using diffraction; IUCr: Newsletter of the CPD: 1999;21:14−15. (33) Dahle, H.; Garshol, F.; Madsen, M.; Birkeland, N. K. Microbial community structure analysis of produced water from a hightemperature North Sea oil-field. Antonie van Leeuwenhoek 2008, 93, 37−49. (34) Stoeva, M. K.; Nalula, G.; Garcia, N.; et al. Resistance and Resilience of Sulfidogenic Communities in the Face of the Specific Inhibitor Perchlorate. Front. Microbiol.. 2019, 10, 654, DOI: 10.3389/fmicb.2019.00654. (35) Gardner, L. R.; Stewart, P. S. Action of glutaraldehyde and nitrite against sulfate-reducing bacterial biofilms. J. Ind. Microbiol. Biotechnol. 2002, 29, 354−360. (36) Mehta-Kolte, M. G.; Loutey, D.; Wang, O.; et al. Mechanism of H2S oxidation by the dissimilatory perchlorate-reducing microorganism Azospira suillum PS. mBio. 2017, 8, No. e02023-16. (37) Carlström, C. I.; Loutey, D. E.; Wang, O.; et al. Phenotypic and Genotypic Description of Sedimenticola selenatireducens Strain CUZ, a Marine (Per)Chlorate-Respiring Gammaproteobacterium, and Its Close Relative the Chlorate-Respiring Sedimenticola Strain NSS. Appl. Environ. Microbiol. 2015, 81, 2717−2726. (38) Flood, B. E.; Jones, D. S.; Bailey, J. V. Sedimenticola thiotaurini sp. Nov., a sulfur-oxidizing bacterium isolated from salt marsh sediments, and emended descriptions of the genus sedimenticola and sedimenticola selenatireducens. Int. J. Syst. Evol. Microbiol. 2015, 65, 2522−2530. (39) Zuo, G.; Roberts, D. J.; Lehman, S. G.; Jackson, G. W.; Fox, G. E.; Willson, R. C. Molecular assessment of salt-tolerant, perchlorate- and nitrate-reducing microbial cultures. Water Sci. Technol. 2009, 60, 1745−1756. (40) Marangon, J.; Paes De Sousa, P. M.; Moura, I.; Brondino, C. D.; Moura, J. J. G.; Gonzalez, P. J. Substrate-dependent modulation of the´ enzymatic catalytic activity: Reduction of nitrate, chlorate and perchlorate by respiratory nitrate reductase from Marinobacter hydrocarbonoclasticus 617. Biochim. Biophys. Acta, Bioenerg. 2012, 1817, 1072−1082. (41) Stepanov, V. G.; Xiao, Y.; Lopez, A. J.; Roberts, D. J.; Fox, G. E. Draft Genome Sequence of Marinobacter sp. Strain P4B1, an Electrogenic Perchlorate-Reducing Strain

Isolated from a Long-Term Mixed Enrichment Culture of Marine Bacteria. Genome Announce. 2016, 4, No. e01617-15. (42) Okpala, G. N.; Chen, C.; Fida, T.; Voordouw, G. Effect of thermophilic nitrate reduction on sulfide production in high temperature oil reservoir samples. Front. Microbiol. 2017, 8, 1573. (43) Okabe, S.; Nielsen, P. H.; Characklis, W. G. Factors affecting microbial sulfate reduction by Desulfovibrio desulfuricans in continuous culture: Limiting nutrients and sulfide concentration. Biotechnol. Bioeng. 1992, 40, 725−734. (44) Greene, E. A.; Hubert, C.; Nemati, M.; Jenneman, G. E.; Voordouw, G. Nitrite reductase activity of sulphate-reducing bacteria prevents their inhibition by nitrate-reducing, sulphide-oxidizing bacteria. Environ. Microbiol. 2003, 5, 607−617. (45) Kaster, K. M.; Grigoriyan, A.; Jennneman, G.; Voordouw, G. Effect of nitrate and nitrite on sulfide production by two thermophilic, sulfate-reducing enrichments from an oil field in the North Sea. Appl. Microbiol. Biotechnol. 2007, 75, 195−203. (46) Druhan, J. L.; Bill, M.; Lim, H.; et al. A large column analog experiment of stable isotope variations during reactive transport: II. Carbon mass balance, microbial community structure and predation. Geochim. Cosmochim. Acta 2014, 124, 394−409. (47) Martinez-Ruiz, F.; Jroundi, F.; Paytan, A.; Guerra-Tschuschke, I.; Abad, M. D. M.; Gonzalez-Mun˜oz, M. T. Barium bioaccumulation by bacterial biofilms and implications for Ba cycling and use of Ba proxies. Nat. Commun. 2018, 9, 1619. (48) Ross, N.; Novakowski, K. S.; Lesage, S.; Deschenes, L.; Samson,ˆ R. Development and resistance of a biofilm in a planar fracture during biostimulation, starvation, and varying flow conditions. J. Environ. Eng. Sci. 2007, 6, 377−388. (49) Bozorg, A.; Sen, A.; Gates, I. D. A new approach to model the spatiotemporal development of biofilm phase in porous media. Environ. Microbiol. 2011, 13, 3010−3023. (50) Kildsgaard, J.; Engesgaard, P. Tracer tests and image analysis of biological clogging in a Two-Dimensional sandbox experiment. Groundwater Monit. Rem. 2002, 22, 60−67. (51) Kolter, R.; Greenberg, E. P. The superficial life of microbes. Nature 2006, 441, 300−302. (52) Ross, N.; Villemur, R.; Deschenes, L.; Samson, R. Clogging of aˆ limestone fracture by stimulating groundwater microbes. Water Res. 2001, 35, 2029−2037. (53) Arnon, S.; Adar, E.; Ronen, Z.; Yakirevich, A.; Nativ, R. Impact of microbial activity on the hydraulic properties of fractured chalk. J. Contam. Hydrol. 2005, 76, 315−336. (54) Arnon, S.; Ronen, Z.; Adar, E.; Yakirevich, A.; Nativ, R. Twodimensional distribution of microbial activity and flow patterns within naturally fractured chalk. J. Contam. Hydrol. 2005, 79, 165−186. (55) Nelson, P. H. Pore-throat sizes in sandstones, tight sandstones, and shales. AAPG Bull. 2009, 93, 329−340.